High Entropy Alloys & Materials
https://doi.org/10.1007/s44210-023-00023-x

ORIGINAL PAPER

Combinatorial Alloy Design and Microstructure Evolution in Laser-cladded Al–Co–Cr–Fe–Ni–Ti Compositionally Complex Alloys

J. Kaspar[1] · A. Hilhorst[2] · L. Gerdt[1] · M. Müller[1] · M. Heidowitzsch[1] · M. Kuczyk[1,3] · A. M. Bettanini[2] · P. J. Jacques[2] · M. Zimmermann[1,3] · C. Leyens[1,3]

Received: 29 August 2023 / Accepted: 10 October 2023

Abstract
In this work, we propose a strategy for high-throughput design and development of compositionally complex alloys combining theoretical and experimental alloy screening. This methodology was applied for the exploration of the $(Co_2CrFeNi_2)_{1\text{-}x\text{-}y}Ti_xAl_y$ subsystem of so-called high entropy superalloys in the Al–Co–Cr–Fe–Ni–Ti alloy system. Alloy design was guided by thermodynamic calculations based on the CALPHAD approach. The evolution of the microstructure with increasing Al and Ti content was analyzed in the as-built, homogenized and age-hardened conditions by means of scanning electron microscopy, energy-dispersive X-ray spectroscopy and electron backscattered diffraction. Additionally, the evolution of the sample hardness with increasing Al and Ti contents was determined for all conditions. Based on the experimental results, the reliability of the CALPHAD calculations was assessed. Generally, a good agreement between calculations and experiments is achieved in the homogenized state. In the aged conditions, the CALPHAD predictions of the precipitation processes are partly inaccurate and need improvement. Optimal Al and Ti concentrations are derived for age hardening through $L1_2$ and combined $L1_2 + B2$ precipitations.

Keywords CALPHAD-aided alloy design · High entropy superalloys · High-throughput screening · Laser metal deposition

Introduction

The design concept of high entropy alloys (HEAs) and compositionally complex alloys (CCAs) based on several major elements instead of a single base element has stimulated the exploration of an immense compositional space for the development of functional and structural metallic materials potentially with superior properties and performance [1–4]. Due to their high mixing entropy, HEAs typically form dense close-packed structures such as face-centered cubic (FCC), body-centered cubic (BCC) and hexagonal close-packed (HCP). Some of these single-phase HEAs have shown promising properties such as high ductility, work hardenability, fracture toughness and damage tolerance, especially in the cryogenic to room-temperature range [5–7]. However, single-phase HEAs, especially with FCC structure, show typically insufficient strength for structural applications to compete with conventional metals such as steels or Al-, Ti- or Ni-based alloys to find their way into applications. For this reason, the HEA research has no longer been restricted to single-phase structures but generalized to CCAs that exhibit microstructures with two or more phases. Utilizing different phase transformations including spinodal decomposition, precipitation and massive transformation, design concepts such as dual-phase [8–11], eutectic [12–14] and precipitation-hardened CCAs [15–20] quickly emerged.

Due to their extremely high melting points, refractory high entropy alloys (RHEAs) with BCC crystal structures are regarded as the most promising structural materials for high-temperature applications [3, 21]. However, the development of RHEAs is still at a very early stage and the right balance between room-temperature ductility and high-temperature strength and oxidation resistance has still to be found [21–24]. In contrast, precipitation-strengthened CCAs based on Co–Cr–Fe–Ni and additionally containing smaller amounts of $L1_2$ (γ')-forming elements such as Al, Ti and Nb

---

✉ J. Kaspar
joerg.kaspar@iws.fraunhofer.de

[1] Fraunhofer Institute for Material and Beam Technology IWS, Dresden, Germany

[2] UCLouvain, Louvain-la-Neuve, Belgium

[3] TU Dresden, Dresden, Germany

are much further developed and currently appear more promising for high-temperature applications [25–28]. Relying on the same main strengthening mechanism of ordered $L1_2$ precipitations in a FCC matrix as conventional Ni-based and Co-based superalloys [29], these CCAs have been named high entropy superalloys (HESAs) [30]. Very recent work explored the composition and temperature stability ranges of the ($\gamma+\gamma$') phase field applying the CALPHAD method [25, 31, 32]. In order to avoid the formation of detrimental intermetallic phases such as sigma phase (σ), Ni_3Ti (η), Ni_2AlTi (Heusler phase $L2_1$) and NiAl (β), there are compositional limits for HESAs constituents. According to Joseph et al. [32], the combined (Al + Ti) content should be below 18 at% to achieve a complete and stable ($\gamma+\gamma$') phase composition. Furthermore, to avoid intermetallic phase formation, the authors and Rieger et al. [31] predicted compositional limits for the combined amounts of Co, Cr and Fe for HESAs that are in the range between 50 and 80 at% and mainly depend on the combined (Al + Ti) content. Within the compositional boundaries for a complete ($\gamma+\gamma$') two-phase region, the volume fraction of γ'-phase and hence the strength of HESAs both increase with the (Al + Ti)-content [32, 33]. Generally, Al/Ti ratios in the region of Al/Ti = 1 lead to better mechanical properties than lower and higher Al/Ti ratios because the lattice misfit between γ and γ' phases as well as the phase fraction and thermal stability of the γ'-phase is higher in the former case [25, 34–36]. Similarly, phase fraction and stability range of the γ'-phase also rise with increasing Ni content [19, 25]. Al–Co–Cr–Fe–Ni–Ti HESAs can exhibit excellent strength-ductility combination up to temperatures of 800 °C that outperform commercial superalloys but without the use of scarce and critical elements, such as Re, Ta and W, while achieving lower density [15, 16, 26, 27]. Although a considerable progress has been achieved during the last decade, the HESA design and development is still at an early stage and further work is urgently required to bring this type of materials into application. One interesting question is, for instance, if besides the ordered $L1_2$ phase, the ordered BCC B2 phase could also be a promising secondary phase to strengthen FCC-based CCAs [26, 31]. It is well known that the BCC B2 phase forms if more than 10 at% of Al are added in Co–Cr–Fe–Ni-based CCAs [37, 38]. As fine and heterogeneous precipitates, the BCC B2 phase can significantly increase the room-temperature yield strength [39]. However, reports on the high-temperature mechanical properties and thermal stability of B2-strengthened CCAs are still missing so that the potential of this design strategy cannot be assessed today.

Two of the major challenges on the way to HEAs/CCAs applications are, on the one hand, the insufficient availability, quality, as well as high cost of raw materials and, on the other hand, the complex and restricted manufacturability and processability [40, 41]. For this reason, HEAs/CCAs are normally synthesized only in very small quantities if manufactured by conventional cast and wrought routes based on arc melting and further thermomechanical processing. In this context, additive manufacturing (AM), particularly laser-based direct energy deposition (L-DED), also referred to as laser cladding or laser metal deposition (LMD) offers practical and very promising solutions. One of the first and most extensively explored CCA system synthesized by L-DED was Al–Co–Cr–Fe–Ni [42–46]. This work demonstrates that L-DED is a suitable and versatile method to synthesize transition metal CCAs. Moreover, L-DED utilizing in situ alloying of different pre-alloyed or elemental powders has been developed to a powerful and reliable tool for rapid HEA/CCA design and development [45, 47–51]. In the Al–Co–Cr–Fe–Ni–Ti CCA system, mainly compositions with higher Al and Ti contents were manufactured by L-DED [52–57]. Due to the high amounts of Al and Ti, the structure of these laser-fabricated samples mainly consisted of a fine mixture of ordered BCC B2 phase and disordered BCC A2 phase, partly additionally containing some minor amounts of intermetallic phases. In contrast, the synthesis and processing of HESAs containing small amounts of Al and Ti by AM were only scarcely explored. Fujieda et al. utilized electron beam and laser powder bed fusion (EPBF and LPBF) to successfully fabricate a $Co_{1.5}CrFeNi_{1.5}Ti_{0.5}Mo_{0.1}$ CCA [58, 59]. With both AM techniques, room-temperature yield strengths (YS) and ultimate tensile strengths (UTS) in the range of 750–930 MPa and 930–1400 MPa could be achieved, respectively. The authors correlate the mechanical properties with the homogeneous precipitation of very fine ordered phase particles although the type of precipitates is not specifically mentioned. Moreover, Lin et al. compared the microstructure and tensile properties of $Al_{0.2}Co_{1.5}CrFeNi_{1.5}Ti_{0.3}$ HESA processed by LPBF and cast and wrought routes [60]. After aging at 750 °C for 50 h, the YS and UTS at room and high (500 °C) temperatures of the LPBF samples considerably exceeded that of the cast and wrought samples. With a similar contribution to $L1_2$ precipitation strengthening in both conditions, the higher strength could be ascribed to grain refinement and the formation of additional precipitates such as $L2_1$ phase and nano-oxides. The very promising results of this work demonstrated the generally huge potential of AM for HESA synthesis and the urgent need for further scientific work in this field.

In this study, a first approach to develop HESAs based on the Al–Co–Cr–Fe–Ni–Ti CCA system for AM fabrication by a combinatorial design approach consisting of CALPHAD-based thermodynamic calculations and L-DED high-throughput screening was pursued. For this, a compositional field based on $Co_2CrFeNi_2$ with additions of Al and Ti in the range of 0 to 12 at% has been thoroughly explored and the designed and synthesized samples have been analyzed by means of analytical scanning electron microscopy (SEM) and microhardness measurements. By decreasing the content of Fe and Cr relative to Ni and Co with respect to the equimolar CoCrFeNi composition the formation of detrimental phases such as σ-, η- and L2$_1$-phase should be avoided and high-volume fractions of L1$_2$ precipitates achieved. Thereby, the boundaries of the Al and Ti contents have been deliberately extended beyond the stability range of the $(\gamma+\gamma')$ dual-phase field to allow additional B2 phase formation in some of the samples.

Materials and Methods

The (Co$_2$CrFeNi$_2$)$_{1\text{-}x\text{-}y}$Ti$_x$Al$_y$ system was explored using the CALPHAD approach to guide the alloy design with Al and Ti contents ranging from 0 to 12 at% over temperatures ranging from 800 to 1600 K. The CALPHAD computations were performed using ThermoCalc software (version 2022a) with the TCHEA5 and TCNI8 databases, specialized databases for HEA and Ni superalloys, respectively. All phases were considered in the initial calculations. In subsequent calculations, a selection of phases among FCC A1, FCC L1$_2$, Ni$_3$Ti, sigma, BCC A2 and BCC B2 phases has been considered to better correlate with the experimentally observed microstructures. Calculations have been made for thermodynamic equilibrium, melting temperature and Scheil solidification. To enable the experimental high-throughput screening and analysis of the (Co$_2$CrFeNi$_2$)$_{1\text{-}x\text{-}y}$Ti$_x$Al$_y$ system, specimens with a range of Al and Ti contents were fabricated by means of L-DED. This was achieved by printing compositionally graded ~ 2.5-mm-thick wall samples layer by layer. The chemical content was successively changed every five (Ti3Aly) or eight (Al-free, Ti5Aly, Ti8Aly) layers generating areas of distinct compositions with relatively sharp transitions (Fig. 11 in supplementary data). Microstructure and hardness of the respective compositions was then characterized along the building direction of the samples. Table 1 gives a comprehensive overview of the targeted compositions and the corresponding actual compositions of the investigated layers measured by means of SEM–EDS analysis.

The general concept of the strategy is described in a recent publication [49]. The DED machine utilized was an Arnold Ravensburg-type 19,389 MTH. Alloys were fabricated by mixing elemental Ti and Al powders (Al: d$_{10}$ = 50 µm, d$_{90}$ = 100 µm (ECKART TLS GmbH); Ti: d$_{10}$ = 90 µm, d$_{90}$ = 125 µm (Höganäs Germany GmbH)) as well as a pre-alloyed and gas-atomized Co$_2$CrFeNi$_2$ powder (d$_{10}$ = 45 µm, d$_{90}$ = 90 µm (NANOVAL GmbH & Co. KG)). The nominal powder composition of the Co$_2$CrFeNi$_2$

Table 1 Nominal and actual composition measured in the laser-cladded samples by EDS analysis

Layer	Composition	Al [at%]	Ti [at%]	Cr [at%]	Fe [at%]	Co [at%]	Ni [at%]
Ti3	Nominal	–	3.0	16.5	16.5	31.90	32.0
	EDS	–	3.8	16.8	18.7	30.4	30.2
Ti6	Nominal	–	6.0	16.0	16.0	30.9	31.1
	EDS	–	7.2	16.0	15.9	30.4	30.5
Ti9	Nominal	–	9.0	15.5	15.5	29.9	30.1
	EDS	–	9.4	15.7	15.5	29.9	29.5
Ti3Al3	Nominal	3.0	3.0	16.0	16.0	30.9	31.1
	EDS	2.7	3.9	16.2	17.0	30.3	30.0
Ti3Al6	Nominal	6.0	3.0	15.5	15.5	29.9	30.1
	EDS	6.6	3.7	15.3	15.4	29.6	29.4
Ti3Al11	Nominal	11.0	3.0	14.7	14.6	28.3	28.4
	EDS	11.5	4.0	14.5	14.2	27.8	27.9
Ti5Al5	Nominal	5.0	5.0	15.3	15.3	29.6	29.7
	EDS	4.5	5.0	15.6	16.7	29.2	29.0
Ti5Al8	Nominal	8.0	5.0	14.8	14.8	28.6	28.8
	EDS	9.0	5.1	14.7	14.7	28.3	28.2
Ti5Al11	Nominal	11.0	5.0	14.3	14.3	27.6	27.7
	EDS	12.1	5.2	14.1	14.1	27.3	27.2
Ti8Al5	Nominal	5.0	8.0	14.8	14.8	26.6	28.8
	EDS	6.2	9.1	14.6	15.5	27.3	27.1
Ti8Al8	Nominal	8.0	8.0	14.3	14.3	27.6	27.8
	EDS	10.5	9.0	13.8	13.7	26.6	26.2
Ti8Al11	Nominal	11.0	8.0	13.8	13.8	26.7	26.8
	EDS	11.7	8.7	13.5	13.5	26.3	26.1

pre-alloyed powder was Co = 32.9 at%, Cr = 17.0 at%, Fe = 17.0 at%, and Ni = 33.1 at%. Mixing was done in situ during processing. By adjusting the rotational speed and hence the feeding rates of three independent GTV PF 2/2 disk powder feeders (GTV Verschleißschutz GmbH, Germany), the amount of each powder could be tuned and consequently the composition of the respective layer modified. Ten-millimeter-thick plates of stainless steel AISI 304 were used as substrate material.

Deposition was performed with a COAXshield process head (Fraunhofer IWS, Germany) and a 4-kW diode laser LDF 4000–30 (Laserline GmbH, Germany). Figure 1 shows the system set-up. The COAXshield is designed to supply the process with an additional shielding gas ensuring an oxygen content within the process zone below 100 ppm. Additionally, the deposition process was carried out in a shielding gas chamber in order to increase safety during the processing of elemental reactive powders such as Ti and Al.

Table 2 summarizes the process parameters which were kept at a constant level during deposition. For process calibration a customized powder particle sensor was used to measure the three different powder streams. During the deposition process, the different particle streams are first combined in a particle mixing chamber before they are supplied to the coaxial deposition nozzle to achieve a homogeneous mixing of the powders.

Table 2 Process parameters for manufacturing of wall specimens

Parameter		Value
Laser power		500 W
Travel speed		400 mm/min
Laser spot diameter		1.6 mm
Shielding and feeding gas		Ar
Powder mass rate:	Al	0.06–0.29 g/min
	Ti	0.11–0.38 g/min
	$Co_2CrFeNi_2$	4,45–5.14 g/min

For further assessment, samples underwent solution heat treatment at 1423 K for 24 h (HT1) and precipitation hardening at 1000 K for 24 h (HT2). The temperatures for HT1 and HT2 were defined based on CALPHAD calculations, especially with respect to the stability range of the $L1_2$ phase. All specimens were water quenched after the holding time. After each step the microstructure of the specimens with different chemical compositions was characterized by means of SEM analysis. For microstructural characterization JEOL JSM-7800F and JEOL JSM-IT700HR (Jeol, Japan) SEMs with energy-dispersive spectroscopy (EDS) detector Oxford X-Max-80 (Oxford Instruments, UK) and electron backscatter diffraction (EBSD) detector Oxford Symmetry S2 (Oxford Instruments, UK) were used. Hardness HV0.1 measurements were taken by utilizing a LECO AMH-43 tester (LECO, USA).

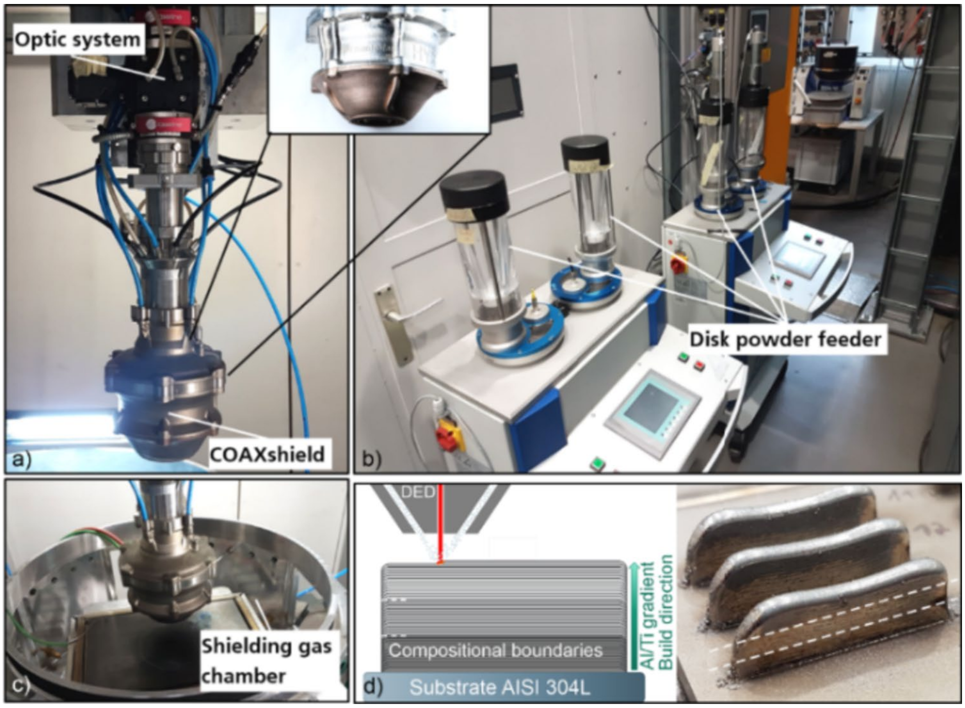

Fig. 1 General experimental set-up of L-DED processing consisting of a Laserline optic system with **a** a COAXshield process head, **b** four independent disk powder feeders (only three were used simultaneously in the current study), **c** a shielding gas chamber. **d** Schematic illustration of the fabrication of compositionally graded $(Co_2CrFeNi_2)_{1-x-y}Ti_xAl_y$ samples with an example of three combinatorial wall specimens. The Al/Ti content changes along the build direction by fine tuning the feeding rates of the respective powders

Results

CALPHAD Calculations

The $(Co_2CrFeNi_2)_{1\text{-}x\text{-}y}Ti_xAl_y$ system was investigated by the CALPHAD approach in the range of 800–1600 K. Figure 2 shows the results of a first screening attempt, including all potentially stable phases included in the TCHEA5 thermodynamic database. This system shows a large region of interest that satisfies the microstructural design criteria of a disordered FCC matrix and strengthening secondary phases such as ordered FCC $L1_2$ and BCC B2. While a high Ti content favors $L1_2$, it also promotes σ-phase at lower temperatures. The Al content does not greatly affect the stability of the $L1_2$ phase. However, the stability of the ordered B2 phase increases mainly with increasing Al content and only slightly with increasing Ti content. The presence of the Ni_3Ti intermetallic is predicted below 1300 K for composition with at least a moderate Ti content and very low amount of Al addition ($<$ 2at%).

As it will be discussed in a later section, the presence of σ-phase could not be confirmed for the investigated experimental compositions. Therefore, the volume phase fractions were recalculated without the σ-phase. Figure 3 shows the results when only FCC, BCC and Ni_3Ti phases were considered. Preventing the formation of σ-phase does not significantly change the predictions for the A1, $L1_2$ and B2 phases. However, a disordered Cr and Fe-rich BCC A2 phase is predicted to be stable below 1000 K and in a similar composition range than the formerly considered σ-phase.

Figure 4 shows the overall calculated fraction of each element in phases present at 1000 K (omitting Ni_3Ti) as a function of the Al and Ti contents. For low Al contents both Al and Ti segregate to the ordered $L1_2$ phase. However, for higher Al contents as soon as the B2 phase is stable, $L1_2$ is depleted of Al and partly also of Ti in favor of the B2 phase. The disordered FCC A1 phase is mostly composed of Cr and Fe, but to a lower extent also contains Co and Ni. Ni segregates mostly in the ordered $L1_2$ phase. Co favors FCC, but there is no significant segregation between the ordered $L1_2$ and disordered A1 phases.

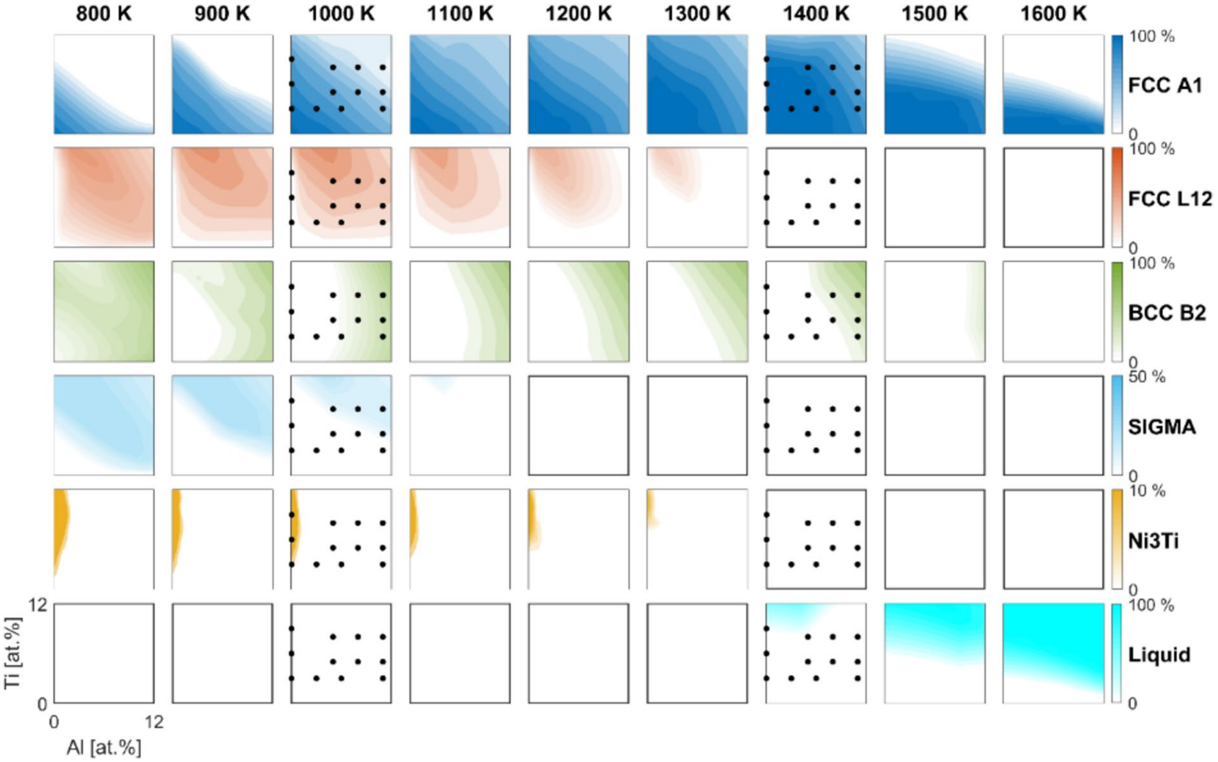

Fig. 2 Prediction of the phase volume fractions in the range of 0 to 12 at% Al and Ti for temperatures between 800 and 1600 K using the CALPHAD approach (TCHEA5 database). Phases that are stable are (disordered) FCC A1, (ordered) FCC L12, (ordered) BCC B2 as well as σ (SIGMA) and Ni3Ti intermetallics. Black dots represent the experimental compositions analyzed in the current study, drawn for 1400 K and 1000 K, the homogenization temperature and aging temperature, respectively

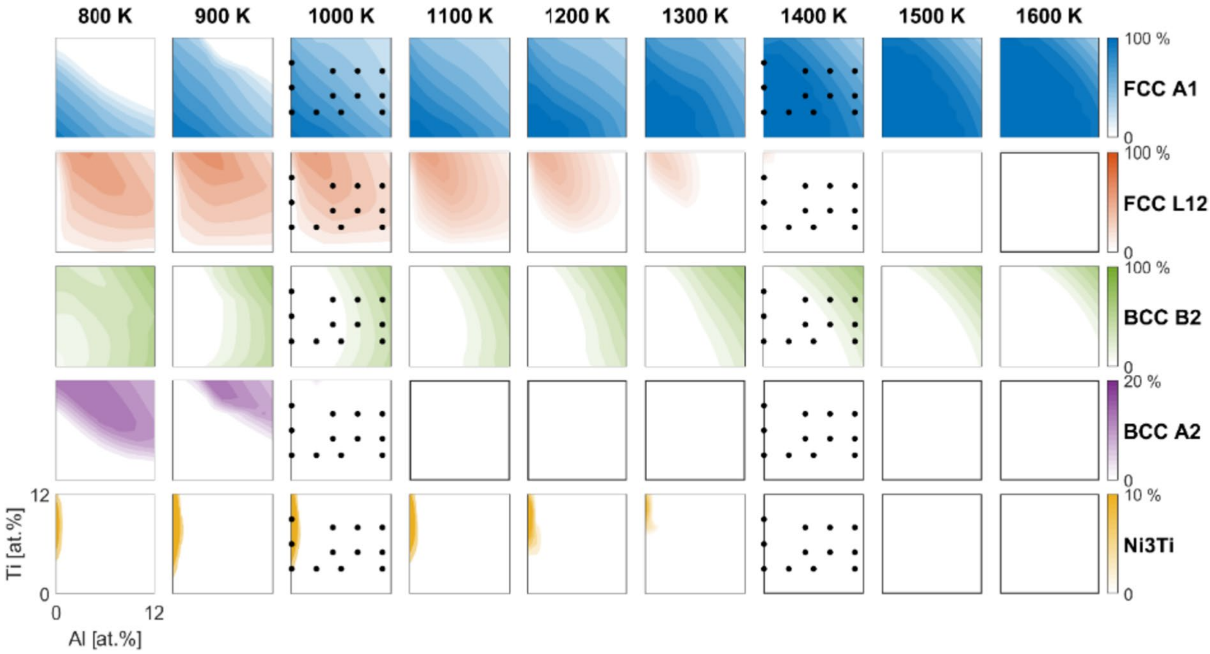

Fig. 3 Prediction of the phase volume fractions in the range of 0 to 12 at% Al and Ti for temperatures between 800 and 1600 K only considering FCC (A1 and L1_2), BCC (A2 and B2) and Ni_3Ti phases using the CALPHAD approach (TCHEA5 database). Black dots represent the experimental compositions analyzed in the current study, drawn for 1400 K and 1000 K, the homogenization temperature and aging temperature, respectively

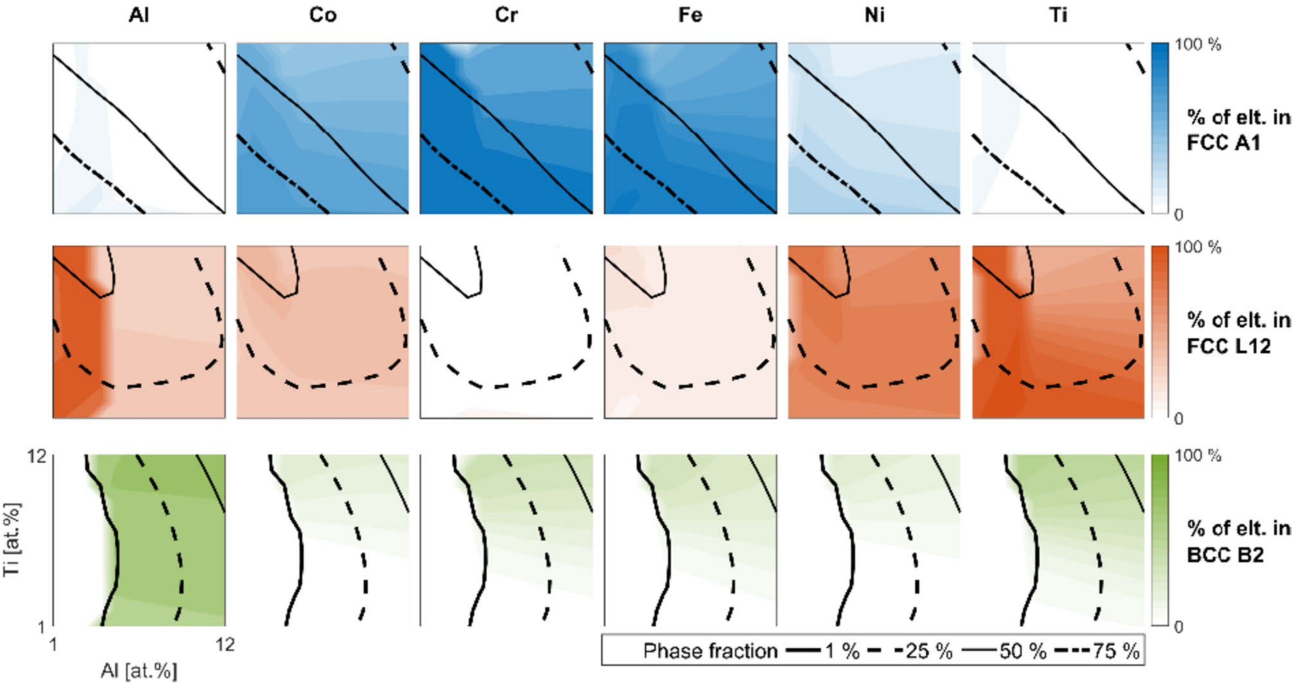

Fig. 4 Segregations of Al, Co, Cr, Fe, Ni and Ti in FCC A1, FCC L12 and BCC B2 phases at 1000 K. Contours corresponding to phase fractions of 1, 25, 50 and 75% are drawn

Microstructural Evolution Through Two-step Heat Treatment: Effect of Al and Ti Content

The first step of the structural analysis was to determine the chemical composition of each individual layer of the wall-type specimens by EDS analysis (Fig. 11, supplementary data). The results of the measured compositions are summarized and also compared with the targeted alloy compositions in Table 1. Largely, the targeted alloy compositions in each layer were met by the proposed L-DED screening approach. Compositional fluctuations are in the range of 1 at%. For compositions containing small amounts of Ti, the actual Ti content is close to 4 at% instead of 3 at%. Moreover, for most compositions, the Al content is slightly higher than intended. To avoid confusion, the designation of these samples has not been changed, nonetheless. The main focus of the current study is on the characterization of the explored system in precipitation-hardened state, due to its practical relevance for application behavior of the investigated alloys. Therefore, the data regarding as-built and solution heat treatment states are placed in supplementary section.

Generally, all samples contain a larger amount of porosity. These pores are typically very small, exhibiting diameters below 1 μm. Porosity formation in the samples is predominantly process-induced and does not depend significantly on alloy composition. It is very likely that the porosity in the laser-cladded samples mainly originates from the residual porosity in the powder feedstock, because all powder feedstock was produced by argon-based gas atomization. Furthermore, it should be noted that in none of the samples cracking could be identified in the as-built and heat-treated conditions. Despite the partly high amounts of Al and Ti alloying the samples appear not to be susceptible to solidification cracking, liquidation cracking and ductility-dip cracking like some Ni-based superalloys [61].

In the as-built condition, the structural evolution in the laser-cladded samples is strongly dependent on the combined (Al + Ti) content (Fig. 12, supplementary data). Generally, and with the exception of the compositions that contain more than 8 at% Al and Ti, respectively, the samples exhibit a characteristic microdendritic solidification structure. Only at low combined (Al + Ti) content ($\lesssim$ 10 at%) the samples are completely single phase, exhibiting a disordered FCC structure. For higher combined (Al + Ti) contents ($\gtrsim$ 10 at%), the BCC B2 phase forms between the FCC dendritic matrix. The BCC B2 phase can easily be identified in the SEM images because it appears darker than the FCC A1 phase. Also, the distinction can easily be done by EBSD and EDS analysis. In contrast to the FCC A1 phase, the BCC B2 phase is strongly enriched in Al, Ti and Ni, but strongly depleted in Cr and Fe. The phase fraction of BCC B2 increases with increasing (Al + Ti) content. In the as-built state, the largest BBC B2 phase fraction was contained in the highest Al- and Ti-alloyed state Ti8Al11. No $L1_2$ phase formation nor precipitation was observed in any of the as-built samples. In samples containing solely Ti and no Al, some minor Ni_3Ti phase formation was identified. Moreover, the B2 phase formation was generally not observed in the Al-free compositions Ti3, Ti6 and Ti9.

The homogenization treatment at 1423 K for 24 h generally transforms the microdendritic structure to an equiaxed coarse-grained structure (Fig. 13, supplementary data). In the Al-free compositions, the Ni_3Ti phase was completely dissolved during homogenization. As a consequence, all three samples (Ti3, Ti6, Ti9) appear to be single-phase FCC A1. Even at higher magnifications no second phase could be found. In the Al and Ti containing samples, the stability range of the BCC B2 phase decreases and the boundary for B2 phase formation shifts to a higher (Al + Ti) content if compared to the as-built state. Accordingly, after homogenization, a fully single-phase FCC A1 structures are now present up to an added (Al + Ti) content of about 12 at%. In order to show the partitioning behavior of the different alloying elements between the A1 and B2 phases, respectively, Table 3 (supplementary data) summarizes the mean chemical composition of all (Al + Ti) containing samples and compares it with the specific composition of the A1 and B2 phases. With the onset of B2 formation with increasing (Al + Ti) content, there is a significant segregation of Al and Ti into B2 leaving A1 depleted in both elements. There is a similar but weaker partitioning behavior of Ni. In contrast, Fe and Cr strongly segregate to A1, leaving B2 strongly depleted in both elements. Only Co appears to be nearly neutral in its partition behavior, slightly favoring the A1 phase.

Figures 5, 6 and 7 illustrate the microstructure evolution depending on the Al and Ti alloying content after homogenization and subsequent precipitation hardening (aging) at 1000 K for 24 h. In all three Al-free compositions (Ti3, Ti6, Ti9), the formation of larger plate-shaped and bright appearing precipitates is evident (Fig. 5j-l). EDS and EBSD analyses confirmed that these relatively large precipitates are Ni_3Ti phase (Figs. 6m and 7e, i). Such Ni_3Ti precipitates predominantly form along the grain boundaries. With increasing Ti content, the size and volume fraction of the Ni_3Ti phase increase. Analyzing the structure of the Al-free samples at higher magnification, the precipitation of another phase becomes visible (Fig. 5l). Similar to the B2 phase, these fine precipitates appear darker than the A1 matrix phase. Because of its different appearance compared to the Ni_3Ti particles, these homogenously distributed precipitates are assumed to be $L1_2$. Although present in all three Al-free compositions, the size and the appearance of $L1_2$ precipitates change as a function of the Ti content. In Ti3, the $L1_2$ precipitates are nearly spherical and smaller than 100 nm. In

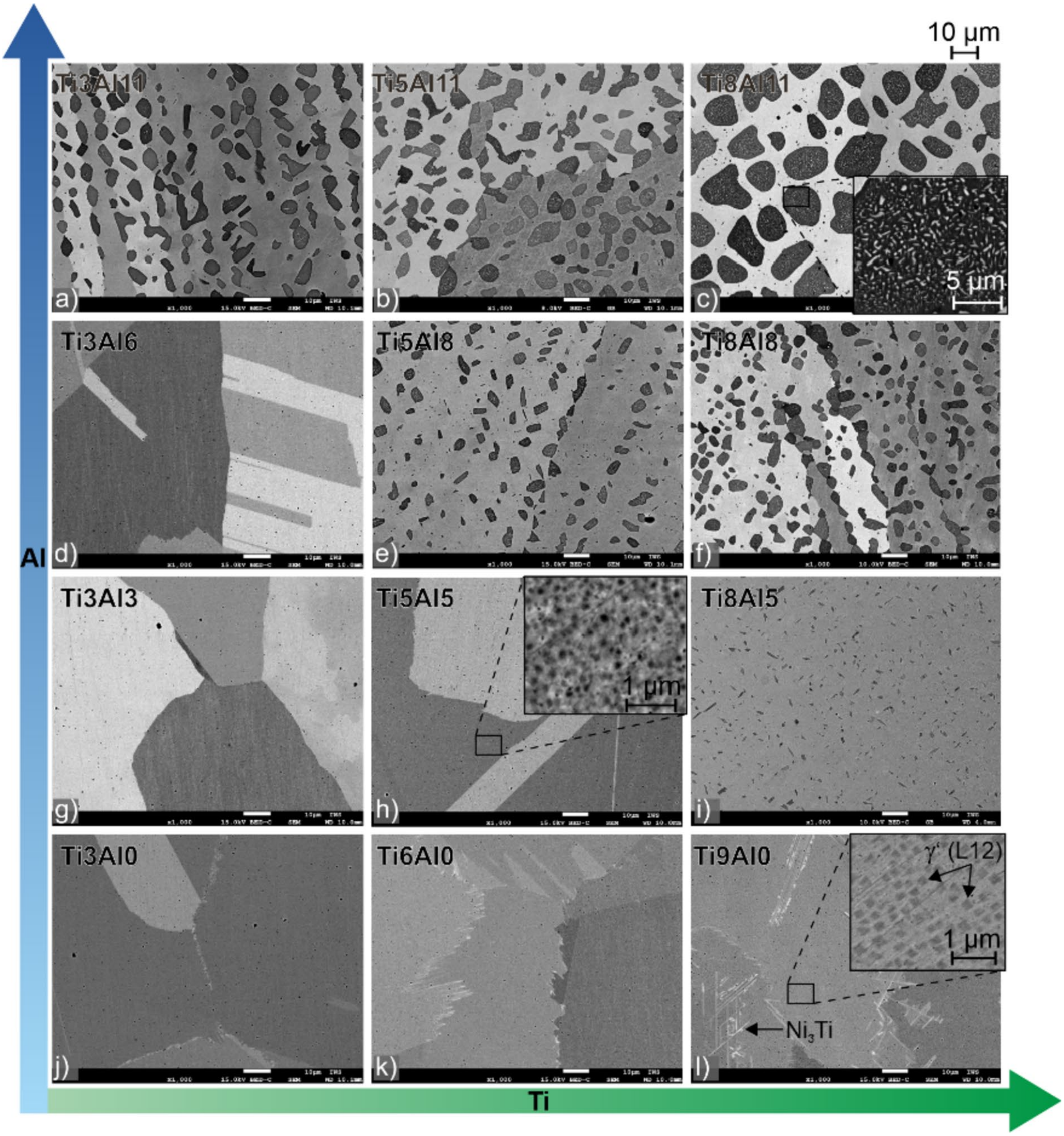

Fig. 5 SEM-BSE micrographs of the samples with different Al and Ti contents after two-step heat treatment HT1 + HT2. Some micrographs contain enlargements in order to represent the occurring different types of precipitation ($L1_2$ in A1 as well as P1 and P2 in B2) during aging

contrast, in Ti6 and Ti9, the $L1_2$ precipitates are cubical and their size reaches about 150 nm and 200 nm, respectively.

In the Al-containing compositions, the active precipitation processes during aging strongly depend on the Al and Ti content. For low combined (Al + Ti) contents ($\lesssim$ 10 at%), i.e., samples that are completely single-phase A1 after homogenization (Ti3Al3, Ti3Al6, Ti5Al5), the precipitation of circular and very fine $L1_2$ particles, smaller than 100 nm, was identified (Fig. 5h). For intermediate (Al + Ti) contents (Al, Ti $\lesssim$ 8 at%), i.e., samples Ti5Al8, Ti8Al5 and Ti8Al8, $L1_2$ precipitation still takes place (Fig. 14, supplementary data). However, similarly to the Al-free samples at intermediate combined (Al + Ti) contents, the $L1_2$ precipitates are again cubical and their size varies between 150 and 200 nm. Remarkably, for all compositions with the highest Al content (11 at%), $L1_2$ precipitation was suppressed and hence could not be observed in Ti3Al11, Ti5Al11 and Ti8Al11. Due to aging at 1000 K, the stability range of the BCC B2 phase increased, i.e., the boundary for B2 phase formation shifted to a lower combined (Al + Ti) content. This is best seen in

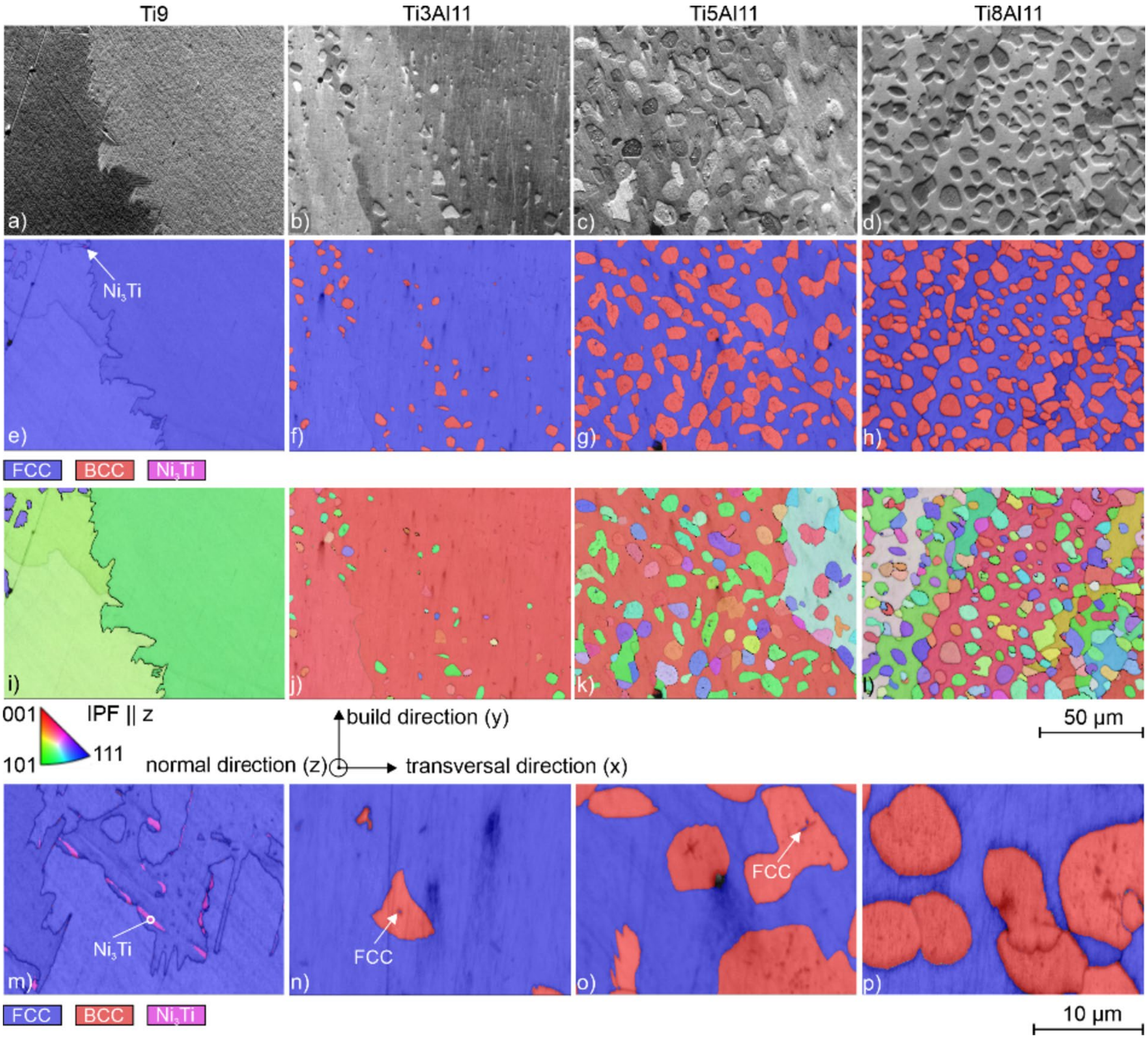

Fig. 6 EBSD analysis of the samples Ti9, Ti3Al11, Ti5Al11 and Ti8Al11 after aging at T = 1000 K (HT2): **a** to **d** forward-scatter detector (FSD) images of the regions of interest; **e** to **h** corresponding EBSD phase mapping, **i** to **l** corresponding orientation mapping (IPF coloring ∥ normal direction); **m**–**p** higher-magnification EBSD phase mapping

the Ti8Al5 sample which is B2-phase-free after homogenization at 1423 K (Fig. 13, supplementary data), yet contains small B2 particles after subsequent aging at 1000 K (Fig. 5i). In the higher Al-alloyed samples (Al ≥ 8 at%), the formation of small particles within the B2 phase is observed after aging (Fig. 5c). Because of their small size, these particles could not be reliably identified by means of combined EDS and EBSD analyses (Figs. 6 and 7). Figure 7 shows that these particles consist of two different phases, both depleted in Al if compared to the B2 matrix composition. However, only one phase (denoted P1) is enriched in Ni, whereas the other one (denoted P2) is enriched in Cr and Fe, but depleted in Ni compared to B2. Finally, it is worth mentioning that σ-phase formation could not be identified in any sample even though CALPHAD calculations clearly predict σ-phase formation at the aging temperature of 1000 K, particularly for higher combined (Al + Ti) contents. Therefore, new calculations excluding the σ-phase formation were conducted, as already described in Sect. "CALPHAD calculations" (Fig. 3).

In order to describe the evolution of the phase composition of the investigated samples from as-homogenized to as-aged conditions, the phase fractions were determined from SEM-BSE micrographs using ImageJ Weka Segmentation tool [62]. Since the phases denoted P1 and P2 could not be separated in the BSE images, the phase fractions of these two phases were displayed together. Furthermore, the L1_2 precipitates were too small to be identified and separated from the A1 phase and hence also displayed together. Finally, for simplicity, Al-free compositions were not considered. The results of phase fraction analysis are

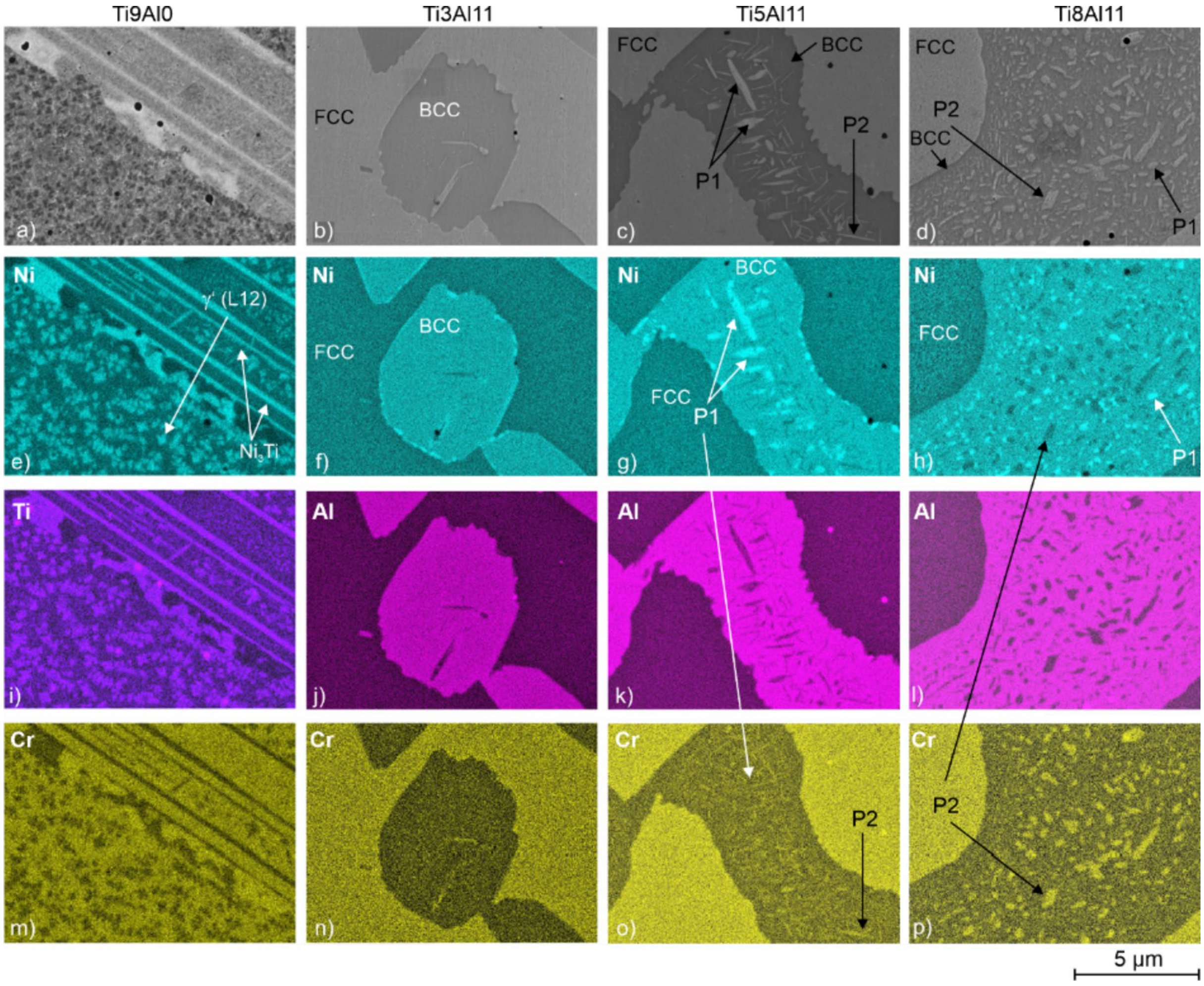

Fig. 7 EDS mapping of the samples Ti9, Ti3Al11, Ti5Al11 and Ti8Al11 after age hardening at T = 1000 K (HT2) for elements Ni, Ti, Al and Cr. a to d SE-images of the regions of interest; e to h Ni distribution, i Ti distribution; j–l Al distribution; m–p Cr distribution

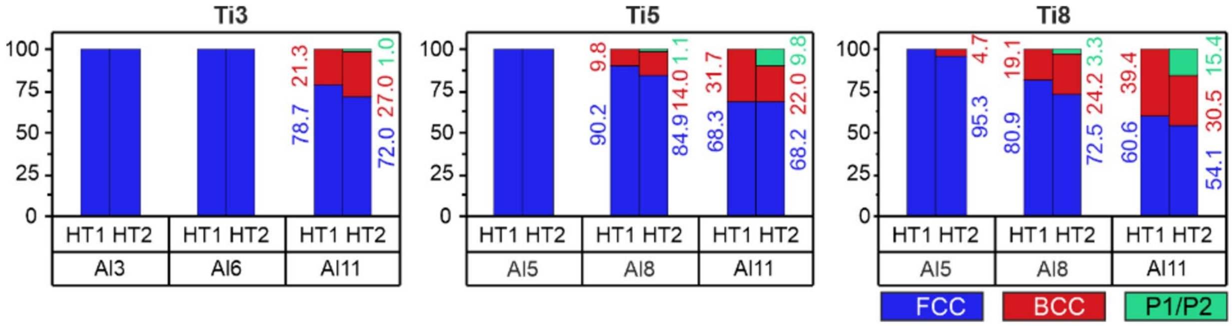

Fig. 8 Calculated phase fractions of FCC, BCC and P1/P2 phases for Al and Ti containing samples after homogenization heat treatment at T = 1423 K (HT1) and after aging at T = 1000 K (HT2)

shown in Fig. 8. Besides the structural changes regarding the precipitation of $L1_2$, P1 and P2, the phase fraction of FCC phases, i.e., ($A1 + L1_2$), is higher in the homogenized state than in the aged condition for all conditions exhibiting both A1 and B2 phases. However, this lower A1 phase fraction is not solely compensated by an increase in B2 phase fraction but also by the formation of the P1 and P2 precipitates within B2.

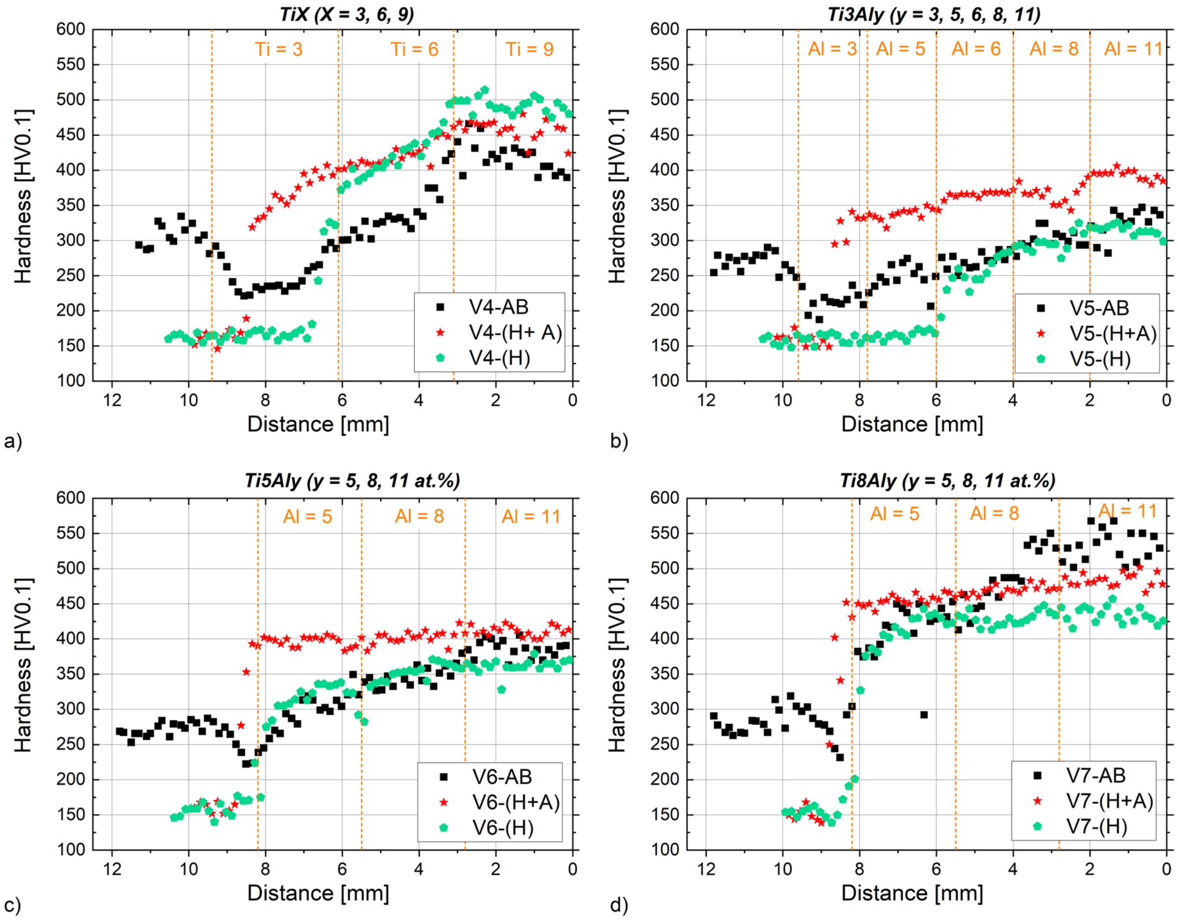

Fig. 9 Hardness line scans along the building direction of the samples with varying Al/Ti contents after laser cladding (AB–as built), homogenization heat treatment (H) and age hardening (H + A) for **a** Al-free, **b** Ti3Aly, **c** Ti5Aly, **d** Ti8Aly samples

Hardness Evolution

The microstructure evolution of the investigated alloys results in significant changes in hardness. The results of the hardness measurements for all three conditions, i.e., as-built, homogenized and precipitation hardened, are summarized in Fig. 9. In the as-built condition, the hardness of the investigated system generally increases with increasing Ti and Al contents. Moreover, Ti seems to have a stronger overall hardening effect than Al. The highest hardness in the as-built state is obtained in samples containing 8 at% and 9 at% Ti and reaches values from 450 to 550 HV. In contrast, the hardness values in samples containing only 3 at% and 5 at% Ti only range from 250 to 400 HV. During homogenization, the Al-containing samples mostly exhibit a slight decrease in hardness. The highest hardness reductions are observed in samples with a very low combined (Al + Ti) content (Ti3Al3, Ti3Al5) and a very high combined (Al + Ti) content (Ti8Al8, Ti8Al11), respectively. In contrast, the Al-free samples show mostly the opposite response to the homogenization treatment. Here, the hardness in the Ti6 and Ti9 samples increases by up to 100 HV when compared to the as-built state. It is worth noting that also during aging the Al-free and Al-containing samples showed an opposite hardening response. In the Al-free samples, only the Ti3 sample showed a strong age-hardening effect, increasing the hardness from 150 HV in the homogenized state to 350 HV in the aged condition. In the higher Ti-alloyed states, Ti6 and Ti9, the hardness does not change significantly. For Ti9, even a slight hardness reduction is observable. Contrary to the Al-free samples, all Al-containing samples exhibit a clearly visible age-hardening response. Generally, the strongest age hardening is obtained in samples with low combined (Al + Ti) content ($\lesssim$ 9 at%). Thus, in the samples Ti3Al3 and Ti3Al6, the increase in hardness during aging is about 200 HV. In contrast, the hardness gain in the samples with medium combined (Al + Ti) content (Ti3Al6, Ti3Al9, Ti3Al11 and Ti5Al5) is only about 100 HV and in samples with a high combined (Al + Ti) content (Ti5Al8, Ti5Al11, Ti8Al5, Ti8Al8 and Ti8Al11) is only about 50 HV. The observed dependence of the aging response on alloying leads to the remarkable result that, for a fixed Ti content, the hardness of the Al-containing HESAs in the homogenized and subsequent aged condition only slightly changes as a function of the Al content. The hardness in the Al-containing HESAs ranges from 350 to 470 HV although the Al content varies between 3 and 11 at% and the Ti content between 3 and 8 at%.

Discussion

Assessment of the CALPHAD Calculations

Applying the proposed CALPHAD screening approach covering all alloy compositions containing between 0 and 12 at% Al and Ti from 800 to 1600 K allowed to identify suitable compositional ranges for (A1 + $L1_2$) dual-phase and (A1 + $L1_2$ + B2) three-phase structures, respectively. Moreover, information about appropriate temperatures for homogenization (1400 K) and aging (1000 K) was derived from these results. The structure in the as-built laser-cladded state is not considered for comparison with the CALPHAD predictions because this state is far from the equilibrium condition assumed by the calculations.

From Figs. 3 and 4, it was derived that 1400 K is well suited for homogenization, because all the phases prone to precipitation at lower temperatures, e.g., $L1_2$, Ni_3Ti, σ and A2, were completely dissolved. For (Al + Ti) $\lesssim$ 10 at%, the structure was predicted to be fully FCC A1 at 1400 K, whereas for (Al + Ti) $\gtrsim$ 12 at%, the ordered B2 phase is also expected to be present. Considering aging, a suitable choice based on the CALPHAD results was found around 1000 K. For higher aging temperatures, the phase fraction and compositional space for $L1_2$ reduce considerably, whereas for lower temperatures, the kinetics of $L1_2$ precipitation slows down, while the risk of unwanted σ- and Ni_3Ti phase formation during aging increases. Joseph et al. [32] calculated (Fe + Cr)-concentration limits for (A1 + $L1_2$) dual-phase regions as a function of the (Al + Ti) content at 1073 K using the TCHEA3 ThermoCalc database. They found that in the range from 6 to 24 at% (Al + Ti), the critical (Fe + Cr) concentration reduces from 40 to 7 at%. For the compositional space in the present work, i.e., (Al + Ti) = 3–19 at% and (Fe + Cr) = 27–33 at%, we calculated the (A1 + $L1_2$) dual-phase field for Al content ranging from 1 to 6 at% and Ti content ranging from 2 to 8 at% at an aging temperature of 1000 K. Within these composition ranges, the highest $L1_2$ content (approx. 35%) is expected for the composition Ti6Al5 containing approx. 30 at% of (Fe + Cr). This is well within the boundary of compositional limits for the (A1 + $L1_2$) dual-phase field as described by Joseph et al. at 1073 K [32]. It has to be pointed out, however, that considering a combined (Al + Ti) concentration might be misleading to predict the stability range of the (A1 + $L1_2$) dual-phase field, if the Al and Ti concentrations differ significantly. While Ti6Al5 is within this dual-phase field, Ti3Al8 and Ti8Al3 are within the ternary phase field of (A1 + $L1_2$ + B2) and (A1 + $L1_2$ + σ), respectively. To extend the (A1 + $L1_2$) dual-phase field to higher (Al + Ti) concentrations and higher temperatures, in order to reach higher $L1_2$ contents and hence achieve higher strengthening and temperature stability, the combined (Fe + Cr) concentration has to be reduced in favor of Ni [25, 31]. Furthermore, it should be explored in future work if Co, which is present in high concentration in the investigated composition ranges despite being a very critical [63] and costly element, can partly be replaced by Fe and not by Ni alone. This would allow to significantly improve the sustainability and reduce the cost of this type of HESAs and hence push them into application.

Comparison of CALPHAD Calculations and Experimental Results

To validate the results of the CALPHAD screening in the $(Co_2CrFeNi_2)_{1\text{-}x\text{-}y}Ti_xAl_y$ HESA system, 12 samples exhibiting different Al/Ti ratios, i.e., six each in the dual-phase and ternary-phase regions, were fabricated by means of in situ laser cladding. Considering the homogenized state (1423 K) with respect to the determined phase fractions, there is generally very good agreement between the calculated and experimentally derived results (Table 4, supplementary data). All samples, including those containing no Al, with (Al + Ti) ≤ 12 at% exhibit fully single-phase A1 structures. Additionally, the B2 structure is stable for (Al + Ti) ≥ 12 at%, whereby the phase fraction of B2 increases with increasing Al content and reaches its highest value for Ti8Al11.

When comparing the results of the aged condition (1000 K), there exist much larger differences regarding the calculated and experimentally derived results. Considering the Al-free conditions, calculations and experiments remain reasonably consistent. Ti3, Ti6 and Ti9 all show an A1 matrix containing fine $L1_2$ precipitates and some larger Ni_3Ti precipitates predominantly forming on the grain boundaries. Although no quantitative data could be derived on the basis of the SEM analysis, the CALPHAD predictions that the $L1_2$ phase content increases with increasing Ti concentration were also observed experimentally. In samples containing Al and Ti, a larger discrepancy between CALPHAD calculations and experiments was observed. This was especially true for the precipitation processes of $L1_2$ within the A1 and of P1 and P2 within the B2 matrix phases, as well as the formation of the σ-phase. Generally, σ-phase formation was identified experimentally in none of the 12 aged samples, even though it had been predicted by CALPHAD for the Ti5Al11, Ti8Al5, Ti8Al8 and Ti8Al11 compositions (Fig. 2). The reason might be that the σ-phase has the highest

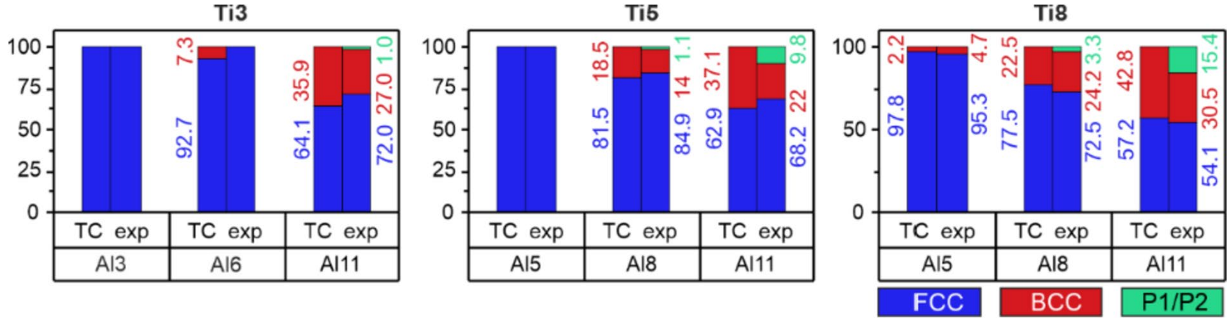

Fig. 10 Comparison of calculated (TC) and experimentally determined (exp) phase fractions of FCC, BCC and P1/P2 phases for Al and Ti containing samples after aging at T = 1000 K referred to as HT1

nucleation barrier of all phase in the A1 matrix and A2, B2 and $L1_2$ can precipitate much more easily during aging [64].

To improve the CALPHAD predictions, the whole compositional space had been recalculated excluding the σ-phase (Fig. 3). In accordance with these calculations, the experimentally determined FCC phase content ($A1 + L1_2$) in the aged state decreases with respect to the homogenized state (Fig. 10 and Table 5, supplementary data). However, the origin of the two Al-depleted phases within the B2 phase, i.e., P1 and P2, has still to be discussed and defined. Because P1 is enriched in Ni and P2 enriched in Cr and Fe, it can be assumed that P1 and P2 are most likely FCC A1 and BCC A2 phase, respectively. However, additional TEM analysis is required and will be performed to confirm this assumption and identify the accompanying phase formation processes. It is worth mentioning that at temperatures below 1000 K, CALPHAD predicts the formation of a BCC A2 phase when excluding the σ-phase. Hence, experimentally, the BCC A2 phase seems to precipitate more easily and/or is more stable than calculated compared to the σ-phase.

According to the obtained CALPHAD results, $L1_2$ precipitation should take place in all Al-containing samples during aging and the $L1_2$ phase content should be mainly controlled by the Ti concentration within the samples. However, we observed $L1_2$ formation only in cladded samples with Al < 11 at%. Moreover, the amount of $L1_2$ precipitation does not seem to strongly depend on the actual Ti concentration. Noticeable differences between calculated data and experimental results were also observed by Rieger et al. [31] for induction-melted, cast and heat-treated HESAs. Using a TCHEA3 database, they reported that generally, the calculated phase fraction of $L1_2$ was overestimated. The overestimation was more pronounced for samples with lower Ni contents (35 at%). Another explanation for the absence of $L1_2$ in samples containing Al = 11 at% could be the strong change in Al, Ti and Ni partitioning behavior once the B2 phase was formed. If, for Al ≤ 8 at%, no or only small amount of B2 phase is formed, there is a good agreement between CALPHAD calculations (Fig. 4) and experiment regarding the strong segregation of Al, Ti and Ni into the $L1_2$ phase and hence the promotion of $L1_2$ precipitation and growth within A1. If, for Al ≥ 8 at%, a significant amount of B2 is formed, especially Al but partly also Ti is supposed to segregate more strongly into B2 than into $L1_2$, but Ni is still predicted to segregate mainly into $L1_2$ (Fig. 4). A strong segregation of Al and Ti into B2 was also observed experimentally in the homogenized state of the laser-cladded samples. However, in contrast to the CALPHAD results, experimentally, B2 was also enriched more strongly with Ni, reducing the Ni content in the A1 phase in which the $L1_2$ precipitation should take place during aging (Table 4, supplementary data). In our opinion, the inaccurate prediction of Ni partitioning for Al ≥ 8 at% is responsible for the overestimation of $L1_2$ precipitation in the CALPHAD calculations for these compositions. Looking at A1 compositions in the homogenized state, it becomes obvious that the Ni and Ti contents in the Al = 11 at% samples are lower than in the Al ≤ 11 at% samples. For instance, in the sample Ti5Al11, the A1 phase contains Al = 7.3, Ti = 3.8 and Ni = 25.6 (at%), whereas in Ti5Al8 it is Al = 7.3, Ti = 4.9 and Ni = 27.5 (at%), respectively. Since it is known that the formation of $L1_2$ requires high Ni/Al ratios in HESAs [18, 32], it can be concluded that favoring the precipitation of $L1_2$ in Al = 11 at% samples requires a significant increase of nominal Ni content and hence a redesign of the composition of the $Co_2CrFeNi_2$ base system. Based on our present results, we show that a critical ratio Ni/Al ≥ 3 has to be fulfilled for $L1_2$ precipitation within FCC A1; i.e., samples containing Al = 11 at% should at least contain Ni = 33 at%.

It is finally remarkable that the shape of the $L1_2$ precipitates changes from spherical to cubical for Ti ≥ 5 at%. This is in agreement with the knowledge that in HESAs the lattice misfit between FCC A1 matrix and coherent $L1_2$ precipitates usually increases with increasing Ti concentrations, thus causing the observed changes in $L1_2$ shape [34].

Correlation Between Structural Evolution and Hardness

Even though in all Al-free samples the hardness strongly depends on the Ti content, the hardness evolution is difficult to correlate with the observed microstructure evolution. Since the as-built state of all three samples (Ti3, Ti6, Ti9) almost completely consists of FCC A1 phase, the hardness increasing with increasing Ti content has to be mainly ascribed to a strong solid solution hardening. While the hardness of Ti3 decreases by about 100 HV due to homogenization, it increases about the same amount in both Ti6 and Ti9 compositions. This is surprising because all three samples exhibit a single-phase A1 structure after homogenization, experiencing a slight coarsening during the transformation from the dendritic to the equiaxed structure. Therefore, a slight decrease rather than an increase of hardness should be expected. Moreover, it is remarkable that a strong age hardening was only observed for Ti3, whereas in Ti6 and Ti9, the hardness did not rise or even slightly dropped during aging despite the fact that $L1_2$ precipitation was observed for all three compositions. To better explain the observed hardness evolution during homogenization and aging, it is supposed that in Ti6 and Ti9, $L1_2$ precipitation already occurred during the cooling from homogenization leading to the observed hardening in the homogenized state. However, this type of precipitates or clusters is probably too small to be detected, even by high-resolution SEM. To prove this assumption, TEM and APT analysis would be required. However, such analysis is beyond the scope of the present work. The work of Fujieda et al. [59] supports this assumption as they found different sized $L1_2$ precipitates in merely homogenized and subsequent air or water-quenched samples of LPBF-fabricated $Co_{1.5}CrFeNi_{1.5}Ti_{0.5}Mo_{0.1}$.

Considering the microstructure and hardness evolution with Al and Ti contents, different strengthening mechanisms such as solid solution, second phase and precipitation hardening are activated. Depending on the amount of Al and Ti alloying and the resulting phase composition in the homogenized and aged conditions, the strengthening mechanisms are separately discussed for $(Al + Ti) \leq 10$ at%, i.e., $A1 + L1_2$ phase composition, $(3, 3) < (Al, Ti) < (10, 10)$ at%, i.e., $A1 + L1_2 + B2$ phase composition and $Al = 11$ at%, i.e., A1 + B2 + A2 (P1 + P2) phase composition.

For a low combined (Al + Ti) content (≤ 10 at%), the solid solution-hardening effect of Al appears to be much lower than of Ti. For instance, for Ti3Al6 and Ti5Al5, the hardness in the as-built and homogenized state is lower than in Ti6, although all samples are single-phase A1. Similarly to Ti3, the age-hardening response due to $L1_2$ precipitation in $(Al + Ti) \leq 10$ at% is very strong, resulting in the hardness increasing by 150 to 200 HV. For a medium combined (Al + Ti) content $(3, 3) < (Al, Ti) < (10, 10)$ at%, there was usually no difference in hardness between the as-built and the homogenized states. Stronger solid solution hardening in addition to second-phase hardening through B2 formation leads to significant higher hardness values (300–400 HV instead of 150–250 HV) than in low (Al + Ti) content compositions. On the other hand, in samples with medium (Al + Ti) content, the age hardening is less pronounced than in samples with low (Al + Ti) content. Consequently, the hardness gain through aging is only in the range of 50–100 HV and generally decreasing with increasing Al and Ti content. Two reasons can be identified for the reduced age-hardening response with increasing Al and Ti content. First, the A1 phase fraction in which $L1_2$ precipitation hardening takes place decreases with increasing Al and Ti content. Second, because of the stronger partitioning of Ni and Ti with increasing Al and Ti content and the resulting depletion of both elements in the A1 phase during homogenization, the $L1_2$ precipitation and hardening is less pronounced. In samples containing 11 at% Al, the later mechanism finally leads to the suppression of the $L1_2$ precipitation in A1. Despite this, the hardness of samples containing $Al = 11$ at% still increases slightly, i.e., ≤ 50 HV, during aging. In Fig. 8, it becomes apparent that the fraction of A1 matrix phase is reduced for the benefit of the combined (B2 + A1/A2) phase fraction during aging. Since the A1 matrix was not precipitation hardened, it should be certainly softer than the ordered B2 phase, which is probably additionally hardened by small particles (assumed to be FCC A1 and BCC A2). To prove this interpretation, it is planned to analyze the individual strengthening behavior of solid solution and precipitation-hardened A1 and B2 phases in this HESA system by nanoindentation measurements in the future.

Alloy Design of Complex Concentrated HESAs

The first alloy development of compositionally complex HESAs was mainly based on knowledge of Ni- and Co-based superalloys. Although sometimes guided by basic thermodynamic calculations, HESA development is still mainly a trial-and-error approach, preparing only a few new alloys with varied chemical compositions by a melting and casting route [16, 17, 30, 65]. Such approach is much too time-consuming to explore the vast compositional space of HEAs, CCAs and hence also HESAs. More recently, fast CALPHAD-based screening approaches searching for single solid solutions have been developed [66–69]. Rieger et al. and Joseph et al. [31, 32] adapted this method to explore the $A1 + L1_2$ dual-phase region in the Al–Co–Cr–Fe–Ni–Ti system and derived very general suggestions for the design of HESAs. Although both authors compared their calculated predictions with a few experiments, the development of $L1_2$-strengthened HESAs is still at an early age. Moreover, combining high-throughput numerical and experimental methods is required for an efficient and accurate HESA development. Haase et al. [47] were the first to suggest and apply such a combinatorial alloy design consisting of thermodynamic calculations and L-DED synthesis, but they applied it initially only for the exploration of a single CoCrFeMnNi alloy. In the present work, we extended this methodology to successfully explore the phase formation in the $(CoCrFeNi)_{1-X}Al_X$ ($0 \leq X \leq 20$ at%) CCA system and find good agreement between CALPHAD predictions and experiments in the homogenized state [45]. In the current work, this approach was further developed [49] and, for the first time, a combined CALPHAD and experimental screening was applied to explore the $(Co_2CrFeNi_2)_{1-x-y}Ti_xAl_y$ CCA system ($0 \leq x,y \leq 12$ at%). Similarly to the former work on the $(CoCrFeNi)_{1-X}Al_X$ system, for the $(Co_2CrFeNi_2)_{1-x-y}Ti_xAl_y$ HESA, there exists a good agreement between calculations and experiments regarding the phase formation at homogenization temperature (Table 4, supplementary data). CALPHAD slightly underestimates the B2 phase fraction for some compositions. As thoroughly discussed in Sect. "Comparison of CALPHAD calculations and experimental results," the difference between calculation and experiment is much larger at aging temperature (1000 K). Still, the A1 + $L1_2$ dual-phase region and the onset of B2 phase formation are described rather adequately by the calculation using the TCHEA5 database. Good agreement between calculations (TCHEA3 database) and experiments for the prediction of phase composition in the duplex A1 + $L1_2$ phase region of the Al–Co–Cr–Fe–Ni–Ti HESA system was also reported in the literature [31, 32, 34]. However, Rieger et al. [31] stated that "a fairly good agreement" is only obtained for Ni-rich compositions. For our compositions, the Ni content is relatively low (about 30 at%). Consequently, for this compositional space, the calculations based on TCHEA5 are still not adequate enough to rely on a pure computational alloy design.

Based on results obtained for the $Co_2CrFeNi_2$ base system, a similar Ti and Al content of 5–6 at% and hence a Al/Ti ratio ≈ 1 appears to allow an optimal strengthening in the A1 + $L1_2$ dual-phase field. Lower (Al + Ti) concentration significantly reduces the solid solution hardening of the HESA, whereas larger (Al + Ti) concentration does not offer further strengthening and lies outside of the A1 + $L1_2$ dual-phase field.

According to the literature, in order to extend the dual-phase region to higher (Al + Ti) concentrations up to 18 at%, and hence allow further strengthening, the Ni content of the base system has to be increased at the expense of the combined (Cr + Fe + Co) concentration [25, 31, 32, 36]. Besides classical $L1_2$ strengthening, a combined strengthening of $L1_2$ and B2 precipitates appears also feasible in the $(Co_2CrFeNi_2)_{1-x-y}Ti_xAl_y$ system but only in a very small compositional range of Ti = 7–8 at% and Al = 4–5 at%. Only for this composition the B2 phase homogenously precipitates as small particles simultaneously with $L1_2$ within the A1 matrix. The highest hardness of all aged samples was achieved for such a composition, e.g., sample Ti8Al5. However, assessing whether samples with this composition also maintain a reasonable ductility, has still to be explored by mechanical testing. Nonetheless, higher concentrations of either Al or Ti considerably coarsen the formed B2 phase. Therefore, for such compositions, a substantial loss of ductility could be expected.

Conclusions

In the current work, a combinatorial alloy design approach consisting of CALPHAD-based thermodynamic calculations and L-DED high-throughput experimental screening and validation was developed to investigate the $(Co_2CrFeNi_2)_{1-x-y}Ti_xAl_y$ subsystem of Al–Co–Cr–Fe–Ni–Ti CCAs. The following conclusions can be drawn:

(1) L-DED utilizing in situ alloying of different pre-alloyed or elemental powders is a very powerful and reliable tool for high-throughput screening, fabrication and validation of new CCAs.

(2) The experimentally determined volume fractions of A1 and B2 phases are in very good agreement with the thermodynamically predicted values of ThermoCalc (TCHEA5 database) at homogenization temperature of about 1400 K.

(3) At the aging temperature of 1000 K, there exist larger discrepancies between CALPHAD calculations and experimental results regarding the precipitation of $L1_2$, A2 and σ-phase, especially for higher Al and Ti concentrations ((Al + Ti) ≥ 12 at%)).

(4) For the chosen $Co_2CrFeNi_2$ base system, a Ti and Al content of 5–6 at% and hence a Al/Ti ratio ≈ 1 appears to allow an optimal strengthening in the A1 + $L1_2$ dual-phase field.

(5) A combined strengthening of $L1_2$ and B2 precipitates appears feasible in a very small compositional range of Al = 4–5 at% and Ti = 7–8 at% and hence a Al/Ti ratio $\lesssim 2$.

Supplementary Information The online version contains supplementary material available at https://doi.org/10.1007/s44210-023-00023-x.

Acknowledgements The authors wish to express special thanks to the colleagues Andrea Ostwaldt, Anna Simon and Anja Mittag for metallographic sample preparation as well as light and electron microscopy analysis.

Funding Open Access funding enabled and organized by Projekt DEAL. The current work was conducted within the M-ERA.NET Project "Novel metallic materials, feedstock and fabrication process for high-performance additive manufactured goods." This project is co-financed with tax funds on the basis of the budget passed by the Saxon state parliament. A.H., A.M.B. and P.J.J. acknowledge the financial support from the NovMatAM project (convention n° 2010095) funded by the Service public de Wallonie, Economie Emploi Recherche (SPW-EER), as well as the help of the LACaMi technological platform of UCLouvain. J.K., L.G., M.K. and M.Z. acknowledge the co-funding of in situ characterization equipment (SEM-EBSD) by European Union and Saxon state parliament within the program "Improvements in research infrastructure and research projects" (application number 100538826).

Data Availability The datasets generated and analyzed during the current study are available from the corresponding author on reasonable request.

Declarations

Conflict of interest The authors have no competing interests to declare that are relevant to the content of this article.

References

1. B. Cantor, Multicomponent and high entropy alloys. Entropy **16**, 4749–4768 (2014). https://doi.org/10.3390/e16094749
2. S. Gorsse, D.B. Miracle, O.N. Senkov, Mapping the world of complex concentrated alloys. Acta Mater. **135**, 177–187 (2017). https://doi.org/10.1016/j.actamat.2017.06.027
3. D.B. Miracle, O.N. Senkov, A critical review of high entropy alloys and related concepts. Acta Mater. **122**, 448–511 (2017). https://doi.org/10.1016/j.actamat.2016.08.081
4. E.P. George, D. Raabe, R.O. Ritchie, High-entropy alloys. Nat. Rev. Mater. **4**(8), 515–534 (2019). https://doi.org/10.1038/s41578-019-0121-4
5. F. Otto, A. Dlouhý, C. Somsen, H. Bei, G. Eggeler, E.P. George, The influences of temperature and microstructure on the tensile properties of a CoCrFeMnNi high-entropy alloy. Acta Mater. (2013). https://doi.org/10.1016/j.actamat.2013.06.018
6. E.P. George, W.A. Curtin, C.C. Tasan, High entropy alloys: a focused review of mechanical properties and deformation mechanisms. Acta Mater. **188**, 435–474 (2020). https://doi.org/10.1016/j.actamat.2019.12.015
7. B. Gludovatz, E.P. George, R.O. Ritchie, Processing, microstructure and mechanical properties of the CrMnFeCoNi high-entropy alloy. JOM **67**(10), 2261–2270 (2015). https://doi.org/10.1007/s11837-015-1589-z
8. Z. Li, F. Körmann, B. Grabowski, J. Neugebauer, D. Raabe, Ab initio assisted design of quinary dual-phase high-entropy alloys with transformation-induced plasticity. Acta Mater. **136**, 262–270 (2017). https://doi.org/10.1016/j.actamat.2017.07.023
9. K.R. Lim, K.S. Lee, J.S. Lee, J.Y. Kim, H.J. Chang, Y.S. Na, Dual-phase high-entropy alloys for high-temperature structural applications. J. Alloy. Compd. **728**, 1235–1238 (2017). https://doi.org/10.1016/j.jallcom.2017.09.089
10. U. Hecht, S. Gein, O. Stryzhyboroda, E. Eshed, S. Osovski, The BCC-FCC phase transformation pathways and crystal orientation relationships in dual phase materials from Al-(Co)-Cr-Fe-Ni alloys. Front. Mater. **7**, 238 (2020). https://doi.org/10.3389/fmats.2020.00287
11. K.G. Pradeep, Y. Deng, Z. Li, D. Raabe, C.C. Tasan, Metastable high-entropy dual-phase alloys overcome the strength–ductility trade-off. Nature (2016). https://doi.org/10.1038/nature17981
12. Y. Lu, Y. Dong, H. Jiang, Z. Wang, Z. Cao, S. GUO, T. Wang, T. Li, P.K. Liaw, Promising properties and future trend of eutectic high entropy alloys. Scr. Mater. **187**(11), 202–209 (2020). https://doi.org/10.1016/j.scriptamat.2020.06.022
13. H. Jiang, K. Han, X. Gao, Y. Lu, Z. Cao, M.C. Gao, J.A. Hawk, T. Li, A new strategy to design eutectic high-entropy alloys using simple mixture method. Mater. Des. **142**, 101–105 (2018). https://doi.org/10.1016/j.matdes.2018.01.025
14. B. Chanda, A. Verma, J. Das, Nano-/ultrafine eutectic in CoCrFeNi(Nb/Ta) high-entropy alloys. Trans. Indian Inst. Met. **71**(11), 2717–2723 (2018). https://doi.org/10.1007/s12666-018-1408-7
15. Y.-J. Chang, A.-C. Yeh, The evolution of microstructures and high temperature properties of AlxCo1.5CrFeNi1.5Tiy high entropy alloys. J. Alloy. Compd. **653**, 379–385 (2015). https://doi.org/10.1016/j.jallcom.2015.09.042
16. H.M. Daoud, A.M. Manzoni, N. Wanderka, U. Glatzel, High-temperature tensile strength of Al10Co25Cr8Fe15Ni36Ti6 compositionally complex alloy (high-entropy alloy). JOM **67**(10), 2271–2277 (2015). https://doi.org/10.1007/s11837-015-1484-7
17. J.Y. He, H. Wang, H.L. Huang, X.D. Xu, M.W. Chen, Y. Wu, X.J. Liu, T.G. Nieh, K. An, Z.P. Lu, A precipitation-hardened high-entropy alloy with outstanding tensile properties. Acta Mater. **102**, 187–196 (2016). https://doi.org/10.1016/j.actamat.2015.08.076
18. Y.-J. Liang, L. Wang, Y. Wen, B. Cheng, Q. Wu, T. Cao, Q. Xiao, Y. Xue, G. Sha, Y. Wang, Y. Ren, X. Li, L. Wang, F. Wang, H. Cai, High-content ductile coherent nanoprecipitates achieve ultrastrong high-entropy alloys. Nat. Commun. **9**(1), 4063 (2018). https://doi.org/10.1038/s41467-018-06600-8
19. T.-K. Tsao, A.-C. Yeh, C.-M. Kuo, H. Murakami, On the superior high temperature hardness of precipitation strengthened high entropy Ni-based alloys. Adv. Eng. Mater. **19**(1), 1600475 (2017). https://doi.org/10.1002/adem.201600475
20. Y.I. Zhao, T. Yang, J.H. Zhu, D. Chen, Y. Yang, A. Hu, C.T. Liu, J.J. Kai, Development of high-strength Co-free high-entropy alloys hardened by nanosized precipitates. Scr. Mater. **148**, 51–55 (2018). https://doi.org/10.1016/j.scriptamat.2018.01.028
21. O.N. Senkov, D.B. Miracle, K.J. Chaput, J.-P. Couzinie, Development and exploration of refractory high entropy alloys—a review. J. Mater. Res. **33**(19), 3092–3128 (2018). https://doi.org/10.1557/jmr.2018.153
22. B. Gorr, F. Müller, M. Azim, H.-J. Christ, T. Müller, H. Chen, A. Kauffmann, M. Heilmaier, High-temperature oxidation behavior of refractory high-entropy alloys: effect of alloy composition. Oxid. Met. **88**(3–4), 339–349 (2017). https://doi.org/10.1007/s11085-016-9696-y
23. B. Gorr, S. Schellert, F. Müller, H.-J. Christ, A. Kauffmann, M. Heilmaier, Current status of research on the oxidation behavior of

refractory high entropy alloys. Adv. Eng. Mater. **23**(5), 2001047 (2021). https://doi.org/10.1002/adem.202001047

24. K.-C. Lo, Y.-J. Chang, H. Murakami, J.-W. Yeh, A.-C. Yeh, An oxidation resistant refractory high entropy alloy protected by CrTaO4-based oxide. Sci. Rep. (2019). https://doi.org/10.1038/s41598-019-43819-x
25. Y.-T. Chen, Y.-J. Chang, H. Murakami, S. Gorsse, A.-C. Yeh, Designing high entropy superalloys for elevated temperature application. Scr. Mater. **187**, 177–182 (2020). https://doi.org/10.1016/j.scriptamat.2020.06.002
26. J.-X. Hou, B.-X. Cao, B. Xiao, Z.-B. Jiao, T. Yang, Compositionally complex coherent precipitation-strengthened high-entropy alloys: a critical review. Rare Met. **41**(6), 2002–2015 (2022). https://doi.org/10.1007/s12598-021-01953-4
27. T. Yang, Y. Zhao, W. Liu, J. Kai, C. Liu, L1 2 -strengthened high-entropy alloys for advanced structural applications. J. Mater. Res. **33**(19), 2983–2997 (2018). https://doi.org/10.1557/jmr.2018.186
28. Y.L. Zhao, T. Yang, Y.R. Li, L. Fan, B. Han, Z.B. Jiao, D. Chen, C.T. Liu, J.J. Kai, Superior high-temperature properties and deformation-induced planar faults in a novel L12-strengthened high-entropy alloy. Acta Mater. **188**, 517–527 (2020). https://doi.org/10.1016/j.actamat.2020.02.028
29. D. Hausmann, C. Solís, L.P. Freund, N. Volz, A. Heinemann, M. Göken, R. Gilles, S. Neumeier, Enhancing the high-temperature strength of a co-base superalloy by optimizing the γ/γ' microstructure. Metals **10**(3), 321 (2020). https://doi.org/10.3390/met10030321
30. A.C. Yeh, T.K. Tsao, Y.J. Chang, K.C. Chang, J.W. Yeh, M.S. Chiou, S.R. Jian, C.M. Kuo, W.R. Wang, H. Murakami, Developing new type of high temperature alloys-high entropy superalloys. Int. J. Metall. Mater. Eng. (2015). https://doi.org/10.15344/2455-2372/2015/107
31. T. Rieger, J.-M. Joubert, M. Laurent-Brocq, L. Perrière, I. Guillot, J.-P. Couzinié, Study of the FCC+L12 two-phase region in complex concentrated alloys based on the Al–Co–Cr–Fe–Ni–Ti system. Materialia **14**, 100905 (2020). https://doi.org/10.1016/j.mtla.2020.100905
32. J. Joseph, M. Senadeera, Q. Chao, K.F. Shamlaye, S. Rana, S. Gupta, S. Venkatesh, P. Hodgson, M. Barnett, D. Fabijanic, Computational design of thermally stable and precipitation-hardened Al–Co–Cr–Fe–Ni–Ti high entropy alloys. J. Alloys Compd. **888**, 161496 (2021). https://doi.org/10.1016/j.jallcom.2021.161496
33. Da. Chen, F. He, B. Han, Q. Wu, Y. Tong, Y. Zhao, Z. Wang, J. Wang, J. Kai, Synergistic effect of Ti and Al on L12-phase design in CoCrFeNi-based high entropy alloys. Intermetallics **110**, 106476 (2019). https://doi.org/10.1016/j.intermet.2019.106476
34. J. Joseph, M. Annasamy, S.R. Kada, P.D. Hodgson, M.R. Barnett, D.M. Fabijanic, Optimising the Al and Ti compositional window for the design of γ' (L12)-strengthened Al–Co–Cr–Fe–Ni–Ti high entropy alloys. Mater. Sci. Eng. A **835**, 142620 (2022). https://doi.org/10.1016/j.msea.2022.142620
35. V. Nandal, R. Sarvesha, S.S. Singh, E.-W. Huang, Y.-J. Chang, A.-C. Yeh, J. Jain, S. Neelakantan, Enhanced age hardening effects in FCC based $Co1_{.5}CrFeNi_{1.5}$ high entropy alloys with varying Ti and Al contents. Materialia **13**, 100823 (2020). https://doi.org/10.1016/j.mtla.2020.100823
36. T. Yang, Y.L. Zhao, Y. Tong, Z.B. Jiao, J. Wei, J.X. Cai, X.D. Han, D. Chen, A. Hu, J.J. Kai, K. Lu, Y. Liu, C.T. Liu, Multicomponent intermetallic nanoparticles and superb mechanical behaviors of complex alloys. Science **362**(6417), 933–937 (2018). https://doi.org/10.1126/science.aas8815
37. Y.-F. Kao, T.-J. Chen, S.-K. Chen, J.-W. Yeh, Microstructure and mechanical property of as-cast, -homogenized, and -deformed AlxCoCrFeNi ($0 \leq x \leq 2$) high-entropy alloys. J. Alloy. Compd. **488**, 57–64 (2009). https://doi.org/10.1016/j.jallcom.2009.08.090
38. W.-R. Wang, W.-L. Wang, S.-C. Wang, Y.-C. Tsai, C.-H. Lai, J.-W. Yeh, Effects of Al addition on the microstructure and mechanical property of AlxCoCrFeNi high-entropy alloys. Intermetallics **26**, 44–51 (2012). https://doi.org/10.1016/j.intermet.2012.03.005
39. S. Dasari, A. Jagetia, Y.-J. Chang, V. Soni, B. Gwalani, S. Gorsse, A.-C. Yeh, R. Banerjee, Engineering multi-scale B2 precipitation in a heterogeneous FCC based microstructure to enhance the mechanical properties of a $Al_{0.5}Co_{1.5}CrFeNi_{1.5}$ high entropy alloy. J. Alloys Compd. **830**, 154707 (2020). https://doi.org/10.1016/j.jallcom.2020.154707
40. J. Bishop-Moser, D. Miracle, High entropy alloy manufacturing: pathway to industrial competitiveness. *MFORSIGHT,* September (2018)
41. M. Baker, Defining pathways for realizing the revolutionary potential of high entropy alloys: a TMS accelerator study. Miner. Metals Mater. Soc. (2021). https://doi.org/10.7449/HEApathways
42. I. Kunce, M. Polanski, K. Karczewski, T. Plocinski, K.J. Kurzydlowski, Microstructural characterisation of high-entropy alloy AlCoCrFeNi fabricated by laser engineered net shaping. J. Alloy. Compd. **648**, 751–758 (2015). https://doi.org/10.1016/j.jallcom.2015.05.144
43. R. Wang, K. Zhang, C. Davies, X. Wu, Evolution of microstructure, mechanical and corrosion properties of AlCoCrFeNi high-entropy alloy prepared by direct laser fabrication. J. Alloy. Compd. **694**, 971–981 (2017). https://doi.org/10.1016/j.jallcom.2016.10.138
44. B. Gwalani, S. Gangireddy, S. Shukla, C.J. Yannetta, S.G. Valentin, R.S. Mishra, R. Banerjee, Compositionally graded high entropy alloy with a strong front and ductile back. Mater. Today Commun. **20**, 100602 (2019). https://doi.org/10.1016/j.mtcomm.2019.100602
45. M. Kuczyk, L. Kotte, J. Kaspar, M. Zimmermann, C. Leyens, Alloy Design and microstructure evolution in the AlxCoCrFeNi alloy system synthesized by laser metal deposition. Front. Mater. **7**, 1 (2020). https://doi.org/10.3389/fmats.2020.00242
46. V. Ocelik, N. Janssen, S.N. Smith, JTh.M. De Hosson, Additive manufacturing of high-entropy alloys by laser processing. JOM **68**(7), 1810–1818 (2016). https://doi.org/10.1007/s11837-016-1888-z
47. C. Haase, F. Tang, M.B. Wilms, A. Weisheit, B. Hallstedt, Combining thermodynamic modeling and 3D printing of elemental powder blends for high-throughput investigation of high-entropy alloys—towards rapid alloy screening and design. Mater. Sci. Eng. A **688**, 180–189 (2017). https://doi.org/10.1016/j.msea.2017.01.099
48. Z. Li, A. Ludwig, A. Savan, H. Springer, D. Raabe, Combinatorial metallurgical synthesis and processing of high-entropy alloys. J. Mater. Res. **33**(19), 3156–3169 (2018). https://doi.org/10.1557/jmr.2018.214
49. M. Müller, C.C. Labisch, L. Gerdt, L. Bach, M. Riede, J. Kaspar, E. López, F. Brueckner, M. Zimmermann, C. Leyens, Multimaterial direct energy deposition: from three-dimensionally graded components to rapid alloy development for advanced materials. J. Laser Appl. **35**(1), 12006 (2023). https://doi.org/10.2351/7.0000788
50. M. Li, J. Gazquez, A. Borisevich, R. Mishra, K.M. Flores, Evaluation of microstructure and mechanical property variations in Al x CoCrFeNi high entropy alloys produced by a high-throughput laser deposition method. Intermetallics **95**, 110–118 (2018). https://doi.org/10.1016/j.intermet.2018.01.021
51. C. Vary, P. Aubry, I. Guillot, P. Grün, J. Kaspar, M. Barbosa, Laser cladding as a flexible exploration tool for the design of cobalt-free hardfacing coatings made of high entropy materials. Procedia

CIRP **111**, 201–204 (2022). https://doi.org/10.1016/j.procir.2022.08.047

52. S. Guan, K. Solberg, D. Wan, F. Berto, T. Welo, T.M. Yue, K.C. Chan, Formation of fully equiaxed grain microstructure in additively manufactured AlCoCrFeNiTi$_{0.5}$ high entropy alloy. Mater. Des. **184**, 108202 (2019). https://doi.org/10.1016/j.matdes.2019.108202
53. M.T. Wall, M.V. Pantawane, S. Joshi, F. Gantz, N.A. Ley, R. Mayer, A. Spires, M.L. Young, N. Dahotre, Laser-coated CoFeNiCrAlTi high entropy alloy onto a H13 steel die head. Surf. Coat. Technol. **387**(5), 125473 (2020). https://doi.org/10.1016/j.surfcoat.2020.125473
54. A. Asabre, M.B. Wilms, A. Kostka, P. Gemagami, A. Weisheit, G. Laplanche, Laser metal deposition of Al$_{0.6}$CoCrFeNi with Ti & C additions using elemental powder blends. Surf. Coat. Technol. **418**, 127233 (2021). https://doi.org/10.1016/j.surfcoat.2021.127233
55. X. Zeng, Z. Liu, G. Wu, X. Tong, Y. Xiong, X. Cheng, X. Wang, T. Yamaguchi, Microstructure and high-temperature properties of laser cladded AlCoCrFeNiTi$_{0.5}$ high-entropy coating on Ti 6Al-4V alloy. Surf. Coat. Technol. **418**, 127243 (2021). https://doi.org/10.1016/j.surfcoat.2021.127243
56. H. Liu, J. Liu, X. Li, P. Chen, H. Yang, J. Hao, Effect of heat treatment on phase stability and wear behavior of laser clad AlCoCrFeNiTi$_{0.8}$ high-entropy alloy coatings. Surf. Coat. Technol. **392**, 125758 (2020). https://doi.org/10.1016/j.surfcoat.2020.125758
57. S. Chen, X. Chen, L. Wang, J. Liang, C. Liu, Laser cladding FeCrCoNiTiAl high entropy alloy coatings reinforced with self-generated TiC particles. J. Laser Appl. (2017). https://doi.org/10.2351/1.4966052
58. T. Fujieda, H. Shiratori, K. Kuwabara, M. Hirota, T. Kato, K. Yamanaka, Y. Koizumi, A. Chiba, S. Watanabe, CoCrFeNiTi-based high-entropy alloy with superior tensile strength and corrosion resistance achieved by a combination of additive manufacturing using selective electron beam melting and solution treatment. Mater. Lett. **189**, 148–151 (2017). https://doi.org/10.1016/j.matlet.2016.11.026
59. T. Fujieda, M. Chen, H. Shiratori, K. Kuwabara, K. Yamanaka, Y. Koizumi, A. Chiba, S. Watanabe, Mechanical and corrosion properties of CoCrFeNiTi-based high-entropy alloy additive manufactured using selective laser melting. Addit. Manuf. **25**, 412–420 (2019). https://doi.org/10.1016/j.addma.2018.10.023
60. W.-C. Lin, Y.-J. Chang, T.-H. Hsu, S. Gorsse, F. Sun, T. Furuhara, A.-C. Yeh, Microstructure and tensile property of a precipitation strengthened high entropy alloy processed by selective laser melting and post heat treatment. Addit. Manuf. **36**, 101601 (2020). https://doi.org/10.1016/j.addma.2020.101601
61. M.M. Attallah, R. Jennings, X. Wang, L.N. Carter, Additive manufacturing of Ni-based superalloys: the outstanding issues. MRS Bull. **41**(10), 758–764 (2016). https://doi.org/10.1557/mrs.2016.211
62. I. Arganda-Carreras, V. Kaynig, C. Rueden, K.W. Eliceiri, J. Schindelin, A. Cardona, H. Sebastian Seung, Trainable weka segmentation: a machine learning tool for microscopy pixel classification. Bioinform. (Oxford, England) **33**(15), 2424–2426 (2017). https://doi.org/10.1093/bioinformatics/btx180
63. A.J. Rosario-Beltré, J. Sánchez-España, V. Rodríguez-Gómez, F.J. Fernández-Naranjo, E. Bellido-Martín, P. Adánez-Sanjuán, J.C. Arranz-González, Critical raw materials recovery potential from spanish mine wastes: a national-scale preliminary assessment. J. Clean. Prod. **407**, 137163 (2023). https://doi.org/10.1016/j.jclepro.2023.137163
64. B. Gwalani, S. Gorsse, D. Choudhuri, M. Styles, Y. Zheng, R.S. Mishra, R. Banerjee, Modifying transformation pathways in high entropy alloys or complex concentrated alloys via thermo-mechanical processing. Acta Mater. **153**, 169–185 (2018). https://doi.org/10.1016/j.actamat.2018.05.009
65. A.M. Manzoni, H.M. Daoud, R. Voelkl, U. Glatzel, N. Wanderka, Influence of w, mo and ti trace elements on the phase separation in al8co17cr17cu8fe17ni33 based high entropy alloy. Ultramicroscopy **159**(Pt 2), 265–271 (2015). https://doi.org/10.1016/j.ultramic.2015.06.009
66. G. Bracq, M. Laurent-Brocq, L. Perrière, R. Pirès, J.-M. Joubert, I. Guillot, The fcc solid solution stability in the Co–Cr–Fe–Mn–Ni multi-component system. Acta Mater. **128**, 327–336 (2017). https://doi.org/10.1016/j.actamat.2017.02.017
67. A. Abu-Odeh, E. Galvan, T. Kirk, H. Mao, Q. Chen, P. Mason, R. Malak, R. Arróyave, Efficient exploration of the high entropy alloy composition-phase space. Acta Mater. **152**, 41–57 (2018). https://doi.org/10.1016/j.actamat.2018.04.012
68. J.M. Rickman, H.M. Chan, M.P. Harmer, J.A. Smeltzer, C.J. Marvel, A. Roy, G. Balasubramanian, Materials informatics for the screening of multi-principal elements and high-entropy alloys. Nat. Commun. **10**(1), 2618 (2019). https://doi.org/10.1038/s41467-019-10533-1
69. P.L. Conway, T. Klaver, J. Steggo, E. Ghassemali, High entropy alloys towards industrial applications: high-throughput screening and experimental investigation. Mater. Sci. Eng. A **830**, 142297 (2022). https://doi.org/10.1016/j.msea.2021.142297